*Acta Oceanol. Sin.*, 2024, Vol. 43, No. 5, P. 41–53
https://doi.org/10.1007/s13131-023-2299-6
http://www.aosocean.com
E-mail: ocean2@hyxb.org.cn

# Three-dimensional thermohaline structure estimation derived from HY-2 satellite data over the Maritime Silk Road and its applications

Zhiqiang Chen[1], Xidong Wang[1, 2], Xiangyu Wu[3]*, Yuan Cao[1], Zikang He[1], Dakui Wang[3], Jian Chen[4]

[1] Key Laboratory of Marine Hazards Forecasting, Ministry of Natural Resources, Hohai University, Nanjing 210024, China

[2] Laboratory for Regional Oceanography and Numercial Modeling, Qingdao Marine Science and Technology Center, Qingdao 266061, China

[3] National Marine Environmental Forecasting Center, Ministry of Natural Resources, Beijing 100081, China

[4] Beijing Institute of Applied Meteorology, Beijing 100029, China

Received 5 November 2023; accepted 15 January 2024



**Abstract**

Estimated ocean subsurface fields derived from satellite observations provide potential data sources for operational marine environmental monitoring and prediction systems. This study employs a statistic regression reconstruction method, in combination with domestic autonomous sea surface height and sea surface temperature observations from the Haiyang-2 (HY-2) satellite fusion data, to establish an operational quasi-real-time three-dimensional (3D) temperature and salinity products over the Maritime Silk Road. These products feature a daily temporal resolution and a spatial resolution of 0.25° × 0.25° and exhibit stability and continuity. We have demonstrated the accuracy of the reconstructed thermohaline fields in capturing the 3D thermohaline variations through comprehensive statistical evaluations, after comparing them against Argo observations and ocean analysis data from 2022. The results illustrate that the reconstructed fields effectively represent seasonal variations in oceanic subsurface structures, along with structural changes resulting from mesoscale processes, and the upper ocean's responses to tropical cyclones. Furthermore, the incorporation of HY-2 satellite observations notably enhances the accuracy of temperature and salinity reconstructions in the Northwest Pacific Ocean and marginally improves salinity reconstruction accuracy in the North Indian Ocean when compared to the World Ocean Atlas 2018 monthly climatology thermohaline fields. As a result, the reconstructed product holds promise for providing quasi-real-time 3D temperature and salinity field information to facilitate fast decision-making during emergencies, and also offers foundational thermohaline fields for operational ocean reanalysis and forecasting systems. These contributions enhance the safety and stability of ocean subsurface activities and navigation.

**Key words:** HY-2 satellite observations, subsurface structures reconstruction, Maritime Silk Road, operational thermohaline product

**Citation:** Chen Zhiqiang, Wang Xidong, Wu Xiangyu, Cao Yuan, He Zikang, Wang Dakui, Chen Jian. 2024. Three-dimensional thermohaline structure estimation derived from HY-2 satellite data over the Maritime Silk Road and its applications. Acta Oceanologica Sinica, 43(5): 41–53, doi: 10.1007/s13131-023-2299-6

## 1 Introduction

Over the past three decades, satellite remote sensing technology advancements have significantly improved our understanding of various physical processes and dynamic mechanisms responsible for changes in sea surface conditions (Isern-Fontanet et al., 2017; Huang et al., 2023). However, a key limitation of most satellite observations is that they monitor only the oceanic surface state, without directly observing changes in its interior (Liu et al., 2017, 2023). Temperature and salinity are crucial parameters for oceanographic research, and serve as the most important physical quantities describing ocean variability. Therefore, establishing a quasi-real-time three-dimensional (3D) temperature and salinity structure of the ocean with long-term continuity holds immense significance for in-depth studies of dynamic and thermal processes within the ocean (Buongiorno Nardelli et al., 2012; Dong et al., 2023), and plays a pivotal role in ensuring the safety and navigation of underwater activities. Accurate estimations of temperature and salinity are essential for predicting ocean conditions, planning routes, and making safety decisions, particularly in operational underwater navigation and production (Burnett et al., 2014). To date, various methods for reconstructing ocean subsurface structures based on satellite remote sensing data have been widely employed, and have helped shed light on the characteristics of subsurface structural changes

Foundation item: The China-ASEAN Marine Cooperation Foundation; the Fundamental Research Funds for the Central Universities under contract No. B210203041; the Postgraduate Research & Practice Innovation Program of Jiangsu Province under contract No. KYCX23_0657; the opening project of the Key Laboratory of Marine Environmental Information Technology of Ministry of Natural Resources under contract No. 521037412.

*Corresponding author, E-mail: wxy@nmefc.cn

(Isern-Fontanet et al., 2008; Ballabrera-Poy et al., 2009; Guinehut et al., 2012; Yan et al., 2021a; Dong et al., 2022; Xie et al., 2022). These methods have expanded our understanding of the ocean system, thereby enabling us to better comprehend its changes and responses (Chen et al., 2020, 2023; He et al., 2021; Liu and Xue, 2022; Su et al., 2023).

Since the late 1980s, researchers have progressively developed techniques to reconstruct quasi-real-time ocean subsurface structures and their variations using satellite remote sensing observations. These methods establish statistical relationships between surface and subsurface ocean states (Hurlburt, 1986; Carnes et al., 1990). The reconstructed fields unveil the oceanic interior circulation, mixing and boundary characteristics (Fox et al., 2002; Guinehut et al., 2004; Mulet et al., 2012; Tang et al., 2022). With the advancement of multi-source high-resolution satellite observations, such methods have matured and provided robust support for marine science and applications (Dash et al., 2012; Martin et al., 2012; Morrow et al., 2019; Ballarotta et al., 2023). Simultaneously, the advancements in domestic autonomous satellite observation fusion technology and the consistent progress of fusion techniques have supplied dependable initial field data for autonomous marine environmental forecast systems. In recent years, domestic fusion gridded products' accuracy and effective resolution have progressively matched those of international mainstream products. Therefore, it is necessary to delve deeper into the potential capability of reconstructing 3D temperature and salinity fields based on domestic autonomous satellite observations, particularly in regions with relatively limited subsurface observational data (Riser et al., 2016).

This study focuses on the region along the Maritime Silk Road (MSR)(0°–52°N, 30°–161°E), which holds strategic importance for marine environmental safety and security (Qiao et al., 2019). This region comprises the South China Sea, the Northwest Pacific Ocean, and the northern Indian Ocean. These subregions' temperature and salinity structures significantly affect the global climate system and regional marine environments (Chen et al., 2011; Nan et al., 2011; Qiu et al., 2014; Yang et al., 2019). We establish an operational quasi-real-time 3D temperature and salinity reconstruction system covering the MSR herein. The system utilizes the Modular Ocean Data Assimilation System (MODAS) (Fox et al., 2002) and domestic operational autonomous high-resolution satellite fusion sea surface temperature (SST) and sea surface height (SSH) observations to reconstruct thermohaline fields. The results may offer a promising avenue for a deeper understanding of the 3D thermohaline structure of the MSR and its evolving characteristics. The remainder of this study is structured as follows. Section 2 provides an overview of the data and reconstruction method. Section 3 evaluates the reconstructed fields based on the Argo observations and ocean model analysis data, along with several product applications in typical ocean dynamic processes at various spatial and temporal scales. The conclusions are given in Section 4.

## 2 Data and methods

### 2.1 *Data*

The quasi-real-time autonomous satellite remote sensing gridded SSH maps, which are essential for the operational reconstruction system, are distributed by the National Satellite Ocean Application Centre (NSOAS). They provide global and regional daily products, including variables such as SSH anomalies, absolute dynamic topography, and geostrophic currents. Our study utilizes the daily global SSH product, which has spatial resolution of 0.25° × 0.25°. Similarly, the required quasi-real-time gridded SST product is also distributed by NSOAS and features the same spatial-temporal resolution as the SSH product.

To establish the surface-subsurface relationships necessary for the reconstruction system, we rely on historical thermohaline profile observations from the World Ocean Database 2018 (WOD18) and Argo observation profiles for the 2002–2021 range. Additionally, to evaluate the reconstructed thermohaline products, we employ Argo thermohaline profiles in 2022, the Operational Mercator global ocean physics analysis and forecast (GOPAF) product from the Copernicus Marine Service (2023), and the World Ocean Atlas 2018 (WOA18) monthly climatology thermohaline fields from the National Centers for Environmental Information (2023). The GOPAF product is centered on the global Nucleus for the European Modelling of the Ocean (NEMO) model. It employs a global tripolar horizontal grid that covers the entire global ocean. It holds on a standard grid at 1/12 degree and 50 standard levels. All variables are on the same grid points, including the daily and monthly 3D potential temperature, salinity and currents information, two-dimensional sea surface level, etc. The daily temperature and salinity datasets are employed herein. Finally, the WOA18 monthly climatology field has a spatial resolution of 0.25° × 0.25° and spans from 89.5°S to 89.5°N and from 179.875°W to 179.875°E.

Additionally, we obtained the 6 h tropical cyclone (TC) track and maximum wind speed data from the International Best Track Archive for Climate Stewardship (IBTrACS, Knapp et al., 2010). This repository compiles recent and historical TC data from various organizations and is recognized as the world's most comprehensive TC dataset.

### 2.2 *Data preprocessing*

Before utilizing historical subsurface thermohaline observation profiles to establish surface-subsurface relationships, rigorous quality control measures are imperative to address potential quality issues associated with *in-situ* observations. The quality control process steps are as follows: (1) observation location/date/time checking; (2) repeat profile checking; (3) pressure reversal and pressure repetition checking; (4) boundary checking of the observed data; and (5) temperature and salinity gradient checking and density stability validation. Following the quality control processes, the original temperature and salinity observation profiles are interpolated to standardized depths. After interpolation, the density stability validation is re-evaluated. Profiles that do not meet the criteria for static stability undergo additional adjustments to eliminate static instability caused by interpolation (Wang et al., 2012a). The standard depths are defined as follows: 0 m, 5 m, 10 m, 15 m, 20 m, 25 m, 30 m, 35 m, 50 m, 75 m, 100 m, 125 m, 150 m, 175 m, 200 m, 250 m, 300 m, 350 m, 400 m, 450 m, 500 m, 600 m, 700 m, 800 m, 900 m, 1 000 m, 1 100 m, 1 200 m, 1 300 m, 1 400 m, 1 500 m, 1 600 m, 1 700 m, 1 750 m, 1 800 m, 1 900 m, 2 000 m, 2 500 m, 3 000 m, 3 500 m, 4 000 m, 4 500 m, 5 000 m, 5 500 m, 6 000 m, 6 500 m, 7 000 m, 7 500 m, 8 000 m, 8 500 m, 9 000 m, for a total of 51 layers.

Similar procedures are applied to the WOA18 monthly climatology fields and Argo observation profiles when evaluating the product. The locations of Argo observations within the MSR region in 2022 are illustrated in Fig. 1, highlighting significant spatial heterogeneity in the observed profile locations, with the South China Sea exhibiting the sparsest observation count.

### 2.3 *Statistic-regression reconstruction method*

MODAS relies on a statistical regression approach to establish a surface-subsurface relationship. This approach is often

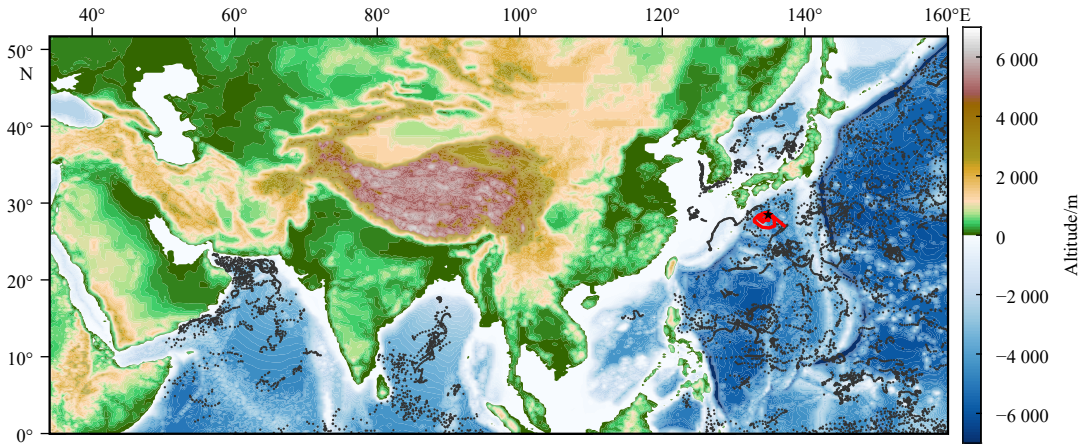


**Fig. 1.** Spatial coverage of the operational reconstruction system. The shaded parts are the altitude in the Maritime Silk Road. The black dots are the locations of Argo observation profiles for 2022. The red line is the trajectory of an Argo buoy (No. 5906510) between May 7, 2022, and December 31, 2022, with a black five-pointed star indicating the observation's starting point.

called the reconstruction model, and is applied to perform subsurface temperature and salinity reconstructions utilizing sea surface information, as described by Fox et al. (2002) and Wang et al. (2012b). The construction of reconstruction model involves the following four key steps: (1) the Empirical Orthogonal Function method is employed to extend the temperature observation profiles at depths where the observations do not reach the seafloor; (2) using the least-squares regression method, profiles containing both temperature and salinity observations are utilized to statistically establish the subsurface temperature-salinity relationship; (3) the temperature-salinity profiles are employed to calculate the steric sea surface height; (4) the historical observation profiles and steric sea surface height are combined with the statistical-regression method to establish the reconstruction model. The above steps are detailed in a study by Wang et al. (2012b). Once the quasi-real-time SSH and SST observations have been inputted into the reconstruction system, the subsurface temperature field is initially established, after which the subsurface salinity field can be reconstructed based on the temperature field and the established subsurface temperature-salinity relationship. Considering the number of subsurface observations and the spatial resolution of the input surface information, we establish a reconstruction model in each calendar month with a 0.25° × 0.25° grid spatial resolution in this study. The reconstructed thermohaline fields have a daily gridded quarter-degree resolution with 51 vertical layers.

### 2.4 *Evaluation method*

The statistical indicator root mean square error (RMSE) is used to evaluate the 3D thermohaline fields quantitatively. The RMSE is sensitive to either very large or very small errors in a set of measurements and thus reflects the precision of the data. Specifically, $\mathrm{RMSE}_T$ and $\mathrm{RMSE}_S$ are defined to quantify the RMSE of temperature and salinity reconstruction fields, respectively, which are calculated as follows:

$$\begin{cases} \mathrm{RMSE}_T = \sqrt{\dfrac{1}{N}\sum\limits_{i=1}^{N}\left(T_{\mathrm{Reconstruction}} - T_{\mathrm{Argo}}\right)^2}, \\ \mathrm{RMSE}_S = \sqrt{\dfrac{1}{N}\sum\limits_{i=1}^{N}\left(S_{\mathrm{Reconstruction}} - S_{\mathrm{Argo}}\right)^2}, \end{cases} \tag{1}$$

where $T_{\mathrm{Reconstruction}}$, $T_{\mathrm{Argo}}$, $S_{\mathrm{Reconstruction}}$, and $S_{\mathrm{Argo}}$ denote the reconstructed temperature field, the temperature of the Argo observation profiles, the reconstructed salinity field, and the salinity of the Argo observation profiles, respectively; $N$ is the number of Argo observation profiles.

The reconstruction skill score (SS) is defined as follows:

$$\mathrm{SS} = 1 - \frac{\mathrm{RMSE}_{\mathrm{Reconstruction}}}{\mathrm{RMSE}_{\mathrm{WOA}}}, \tag{2}$$

where $\mathrm{RMSE}_{\mathrm{Reconstruction}}$ and $\mathrm{RMSE}_{\mathrm{WOA}}$ are the RMSE of the reconstructed field and WOA18 monthly climatology field relative to the Argo observations, respectively. The larger the SS, the better the accuracy of reconstruction fields. SS = 1 is regarded as a perfect skill.

### 2.5 *Calculation of TC-induced temperature anomaly*

Next, we employ the composite analysis method proposed by Mei and Pasquero (2013) to investigate the temperature response in the upper ocean during TC passage. The methodology schematic is illustrated in Fig. 2. Initially, a box centered on the 6-hourly TC location is extended, covering 200 km along the TC path and 2 500 km perpendicular to the path, as depicted in the black and blue shaded portions of Fig. 2. Subsequently, the grid within the extended box is further subdivided into smaller grids with a spatial resolution of 10 km × 10 km. Following this, the detrended upper ocean temperature field, which removes the seasonal signal and the long-term linear trend, is then interpolated into each of the small grids to generate a composite spatial temperature field for each TC location. For each fixed domain, the upper ocean temperature anomaly within a period of –30 d to 30 d relative to TC passage is calculated. This is achieved by subtracting the average temperature field during the month preceding the TC passage. This methodology allows for precisely assessing the upper ocean temperature variations associated with the TC passage (Ma et al., 2018).

## 3 Results

### 3.1 *Quantitative evaluation of reconstructed thermohaline fields*

#### 3.1.1 *Vertical error statistics in MSR*

Figures 3a and b illustrate the vertical profiles of temperature and salinity RMESs of the MODAS reconstructed fields and

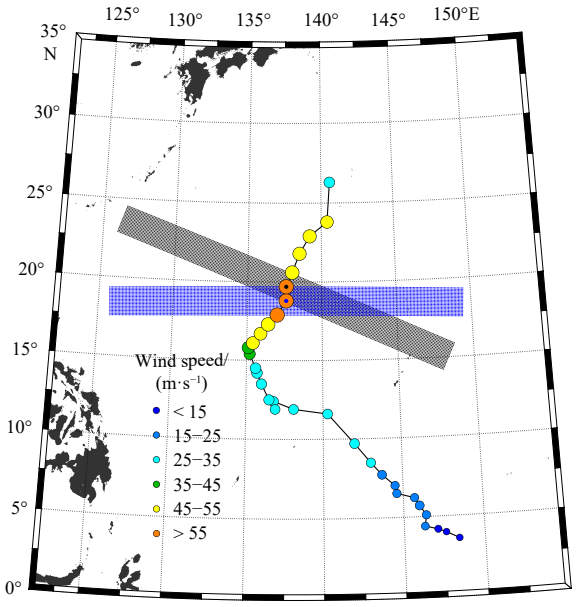


**Fig. 2.** Schematic of the method used to calculate the tropical cyclones (TC)-induced upper oceanic temperature anomalies. The black shaded part represents the study area employed for spatial composite centered on the TC location (the black dot). The spatial resolution of the grid points in this region is 10 km × 10 km. The blue-shaded part, centered around the blue dot, is the same as the black-shaded part, but for an earlier time. The colored dots are the track points at 6 h intervals for TC Malakas in 2022. The size and color of the dots are determined by the TC maximum wind speed (unit: m/s).

WOA18 monthly climatology fields in the Northwest Pacific Ocean (NWP) and North Indian Ocean (NIO) and throughout the MSR region. The reconstruction skill scores of MODAS reconstructed temperature and salinity are also depicted in Fig. 3c. The results show that the most significant temperature reconstruction errors typically appear around the thermocline at depths of approximately 50–300 m, with errors diminishing rapidly below the thermocline depth (Fig. 3a). Temperature and salinity reconstruction errors exhibit distinct variations across different ocean basins, as revealed by Fig. 3 and Table 1.

The maximum mean $RMSE_T$ is 1.35 and 1.47℃ in the MSR and NIO at depths of 50–150 m, respectively, while it is 1.40℃ in the NIO at depths of 150–300 m. The mean $RMSE_T$ for the upper 1 500 m is less than 0.81℃ for various ocean basins (Table 1). In the entire MSR, the maximum $RMSE_T$ is approximately 1.5℃ for the MODAS-reconstructed temperature field upper 1 500 m. This value is generally smaller than that of the climatology temperature field, which locally exceeds 2.0℃ around the thermocline depth (Fig. 3a). The SS of the temperature field holds nearly 0.20 upper 800 m in the NWP and MSR, except for exhibiting a decrement below the thermocline depth of about 200 m. In contrast, the NIO shows only marginal positive SS locally at upper 1 000 m (Fig. 3c).

Regarding the salinity reconstruction, the RMSEs of salinity fields are slightly lower for the MSR and NWP compared to the climatology field, aligning with a mostly positive SS upper 600 m (Figs 3b and c). However, the $RMSE_S$ of MODAS reconstruction is marginally greater than the climatology field below the mixed layer in the NIO, although its value remains below 0.3 (Fig. 3b), leading to a negative SS at almost all depths in the NIO (Fig. 3c). The relatively larger salinity reconstruction errors in the NIO may be associated with factors such as precipitation and runoff-induced seawater desalination, complex temperature-salinity relationships, and the intrusion of high-salinity mode waters.

### 3.1.2 *Spatial distribution of reconstruction errors in the MSR*

Given the complex dynamical regimes within the MSR and the uneven distribution of the Argo observations, we divided the entire area into 4° × 4° subregions to quantitatively evaluate the spatial variability of temperature and salinity reconstruction performance. Please note that the $RMSE_T$ and $RMSE_S$ in this section are the RMSE between reconstructed fields and Argo observations throughout the whole water column in each 4° × 4° subregion. Then, the SS is calculated in each subregion. In Figs 4a–c, we present the spatial distribution of the $RMSE_T$ and SS for both

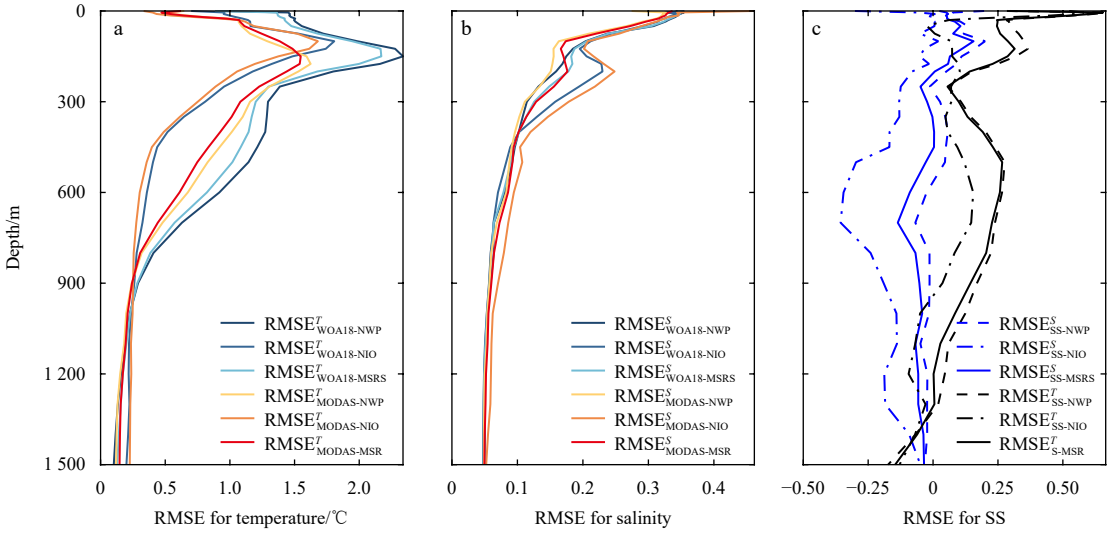


**Fig. 3.** Vertical distributions of root mean square errors (RMSEs) for temperature (a) and salinity (b) of MODAS-reconstructed and WOA18 monthly climatology field in various ocean basins, and the vertical distributions of SS for the reconstructed temperature (black lines) and salinity (blue lines) fields in the NWP, NIO, and MSR, respectively (c). MODAS, Modular Ocean Data Assimilation System; WOA18, World Ocean Atlas 2018; NWP, Northwest Pacific Ocean; NIO, North Indian Ocean; MSR, Maritime Silk Road.

**Table 1.** The mean $RMES_T$ and $RMSE_S$ of MODAS reconstructed fields at various depth ranges in different regions

| Depth/m | $RMES_T$/°C | | | $RMSE_S$ | | |
|---|---|---|---|---|---|---|
| | MSR | NWP | NIO | MSR | NWP | NIO |
| [0, 50) | 0.77 (1.33) | 0.79 (1.41) | 0.69 (1.01) | 0.32 (0.34) | 0.31 (0.34) | 0.35 (0.33) |
| [50, 150) | 1.35 (1.89) | 1.31 (1.98) | 1.47 (1.54) | 0.20 (0.22) | 0.19 (0.22) | 0.23 (0.23) |
| [150, 300) | 1.32 (1.54) | 1.40 (1.66) | 0.97 (1.07) | 0.16 (0.16) | 0.14 (0.14) | 0.22 (0.20) |
| [300, 900) | 0.64 (0.81) | 0.70 (0.90) | 0.37 (0.40) | 0.09 (0.08) | 0.08 (0.08) | 0.10 (0.08) |
| [900, 1 500) | 0.17 (0.17) | 0.15 (0.16) | 0.23 (0.22) | 0.05 (0.05) | 0.05 (0.05) | 0.06 (0.05) |
| [0, 1 500] | 0.79 (1.09) | 0.81 (1.16) | 0.68 (0.79) | 0.17 (0.17) | 0.16 (0.17) | 0.19 (0.18) |

Note: The mean root mean square errors (RMSEs) of WOA18 monthly climatology fields are listed in the parenthesis. MODAS, Modular Ocean Data Assimilation System; WOA18, World Ocean Atlas 2018.

the MODAS-reconstructed and WOA18 monthly climatology fields. The MODAS-reconstructed temperature exhibits lower $RMSE_T$ values than the climatology field in most subregions across the entire water column, with values predominantly below 0.8℃. Larger $RMSE_T$ values are concentrated in nearshore areas that are significantly influenced by topography, including the southern Kuroshio Extension, the Yellow and Bohai seas, the Japan Sea, the northern Arabian Sea, and the southern Indian Peninsula (Figs 4a and b). Most subregions display skill scores exceeding 0, indicating that the reconstruction product generally outperforms the climatology field. Subregions with skill scores above 0.4 are primarily located in the open oceans of the NWP, where the vertical first-order baroclinic mode can properly represent dynamical regimes. Incorporating SSH observation is beneficial for reconstructing subsurface temperature variations induced by the first-order baroclinic mode.

As for salinity reconstruction, in most NWP regions, the MODAS-reconstructed field generally outperforms the climatology field, whereas in the NIO, the performance of the MODAS-reconstructed field is comparable or slightly inferior (Figs 4d–f). This discrepancy can be attributed to the particularity of salinity variations in the NIO. The intense precipitation and runoff events, the strong runoff of the Ganges River into the Bay of Bengal, and the intrusion of high-temperature and high-salinity water from the Somali Current into the Arabian Sea would all decrease the local salinity reconstruction performance, as previously evidenced by He et al. (2021).

### 3.1.3 *Evaluation based on single-point observation profiles*

We selected five individual observation profiles in the NWP and NIO to evaluate the reconstructed vertical profiles. In these profiles, the reconstructed profiles closely match the Argo observations for temperature. This alignment indicates that incorporating satellite observations enhances the accuracy of reconstructing the vertical thermocline profile. Furthermore, the consistency between the MODAS-reconstructed and observation profiles is superior to that between the WOA18 monthly climatology and observation profiles ($a_1$–$a_5$ and $b_1$–$b_5$ in Fig. 5). However, there is notable uncertainty in the reconstruction of salinity vertical profiles, especially in the Somali Sea and northern Arabian Sea within the NIO. In these areas, significant disparities are

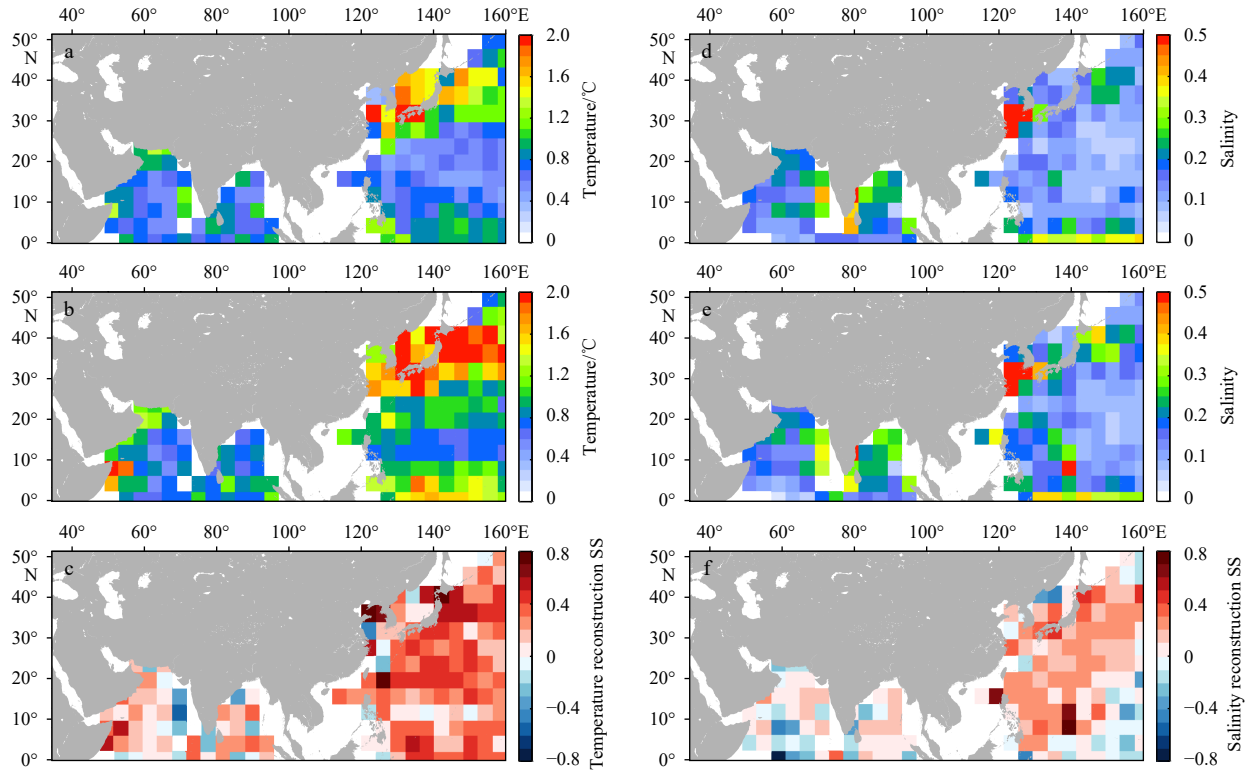


**Fig. 4.** Spatial distributions of $RMSE_T$ of MODAS-reconstructed (a) and WOA18 (b) monthly climatology temperature fields in every 4° × 4° bin, spatial distribution of temperature reconstruction SS in every 4° × 4° bin (c), and spatial distributions of $RMSE_S$ of MODAS-reconstructed (d) and WOA18 (e) monthly climatology salinity fields in every 4° × 4° bin, spatial distribution of salinity reconstruction SS in every 4° × 4° bin (f). RMSE, root mean square error; MODAS, Modular Ocean Data Assimilation System; WOA18, World Ocean Atlas 2018.

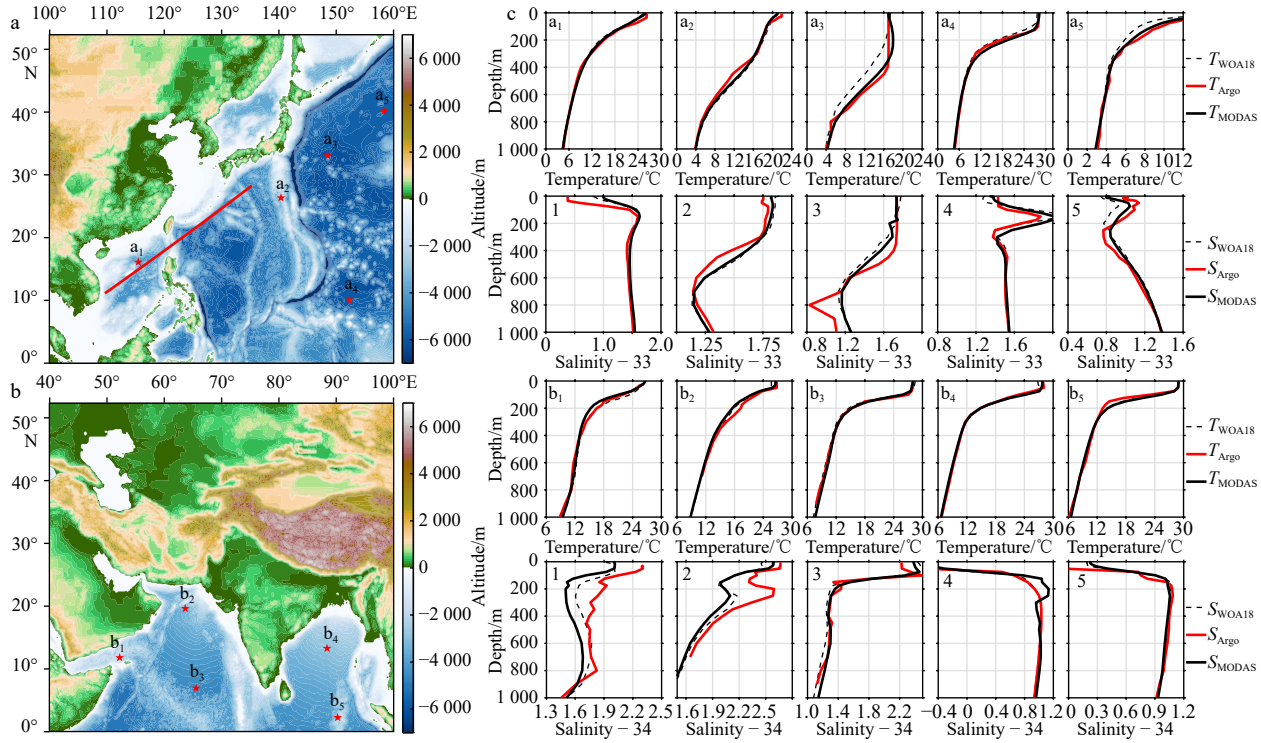


**Fig. 5.** The altitude (shaded part) in the Northwest Pacific Ocean (a) and North Indian Ocean (b), respectively; temperature and salinity vertical profiles for the Argo observed (red lines), the MODAS reconstructed (black solid line), and the WOA18 monthly climatology (black dashed line) in the upper 1 000 m (c). The solid red line in a is the horizontal location of the vertical sections shown in Figs 6 and 7. The red five-pointed stars in a and b represent the locations of the selected Argo observation profiles. $a_1$–$a_5$ and $b_1$–$b_5$ are the mark of these profiles. The temperature and salinity vertical profiles of $a_1$–$a_5$ are shown in the first and second rows in c, and those of $b_1$–$b_5$ showing in the third and last rows in c, respectively. MODAS, Modular Ocean Data Assimilation System; WOA18, World Ocean Atlas 2018.

evident between the observation profiles and both the reconstructed and climatology profiles ($b_1$–$b_5$ in Fig. 5). This variation may be attributed to the limitations of reconstructed salinity in accurately representing the hypersaline seawater resulting from the Somali cold current during winter. Similar to the spatial distribution of $RMSE_S$, the comparison of single-point profiles also demonstrates that the NWP outperforms the NIO in salinity reconstruction (Fig. 5).

### 3.2 *Applications of the reconstructed thermohaline fields*

#### 3.2.1 *Reproducing the thermohaline seasonal variations*

A vertical section is chosen to assess the reconstruction performance in depicting seasonal variations, from southwest to northeast between 110°E and 135°E, crossing through the South China Sea and Luzon Strait, then extending to southern Japan. Figure 6 shows various temperature fields along this section, including MODAS-reconstructed (Fig. 6b) and GOPAF product (Fig. 6b) on the 15th day of every two months from February to December 2022. Figure 6c are the corresponding WOA18 monthly climatology field. The MODAS-reconstructed section closely resembles that of the GOPAF product section regarding the seasonal variation of temperature vertical structure and the isothermal fluctuations caused by mesoscale processes. Conversely, the climatology section exhibits little isothermal variation for the same month. Furthermore, a notable difference emerges in describing thermocline changes of the reconstructed temperature sections on the east and west sides of the Luzon Strait. The west side, corresponding to the South China Sea, features a shallower thermocline depth and a relatively moderate zonal temperature gradient, while the thermocline depth east of the Luzon Strait is much deeper, and displays a stronger zonal temperature gradient with seasonal variations. These characteristics align with the relatively intense temperature variations along the western boundary current. Such a difference is also evident in the GOPAF product sections but is absent in the climatology sections.

Figure 7 illustrates the vertical salinity sections. Although the MODAS-reconstructed salinity sections successfully depict seasonal variations and capture isohaline fluctuations induced by mesoscale processes, they do not substantially improve the salinity reconstruction performance compared to the GOPAF product and WOA18 monthly climatology sections. This may be attributed to the absence of surface salinity observations herein and the limitations of the current reconstruction method, since it relies on the subsurface temperature-salinity relationship to derive the salinity field. These limitations hinder the characterization of high-frequency salinity variability.

#### 3.2.2 *Reconstruction of the mesoscale processes*

An Argo buoy (No. 5906510) recorded the effects of apparent mesoscale processes on the subsurface thermohaline structure in southern Japan between May 7 and December 31, 2022, as revealed by its trajectory, and the results are shown in Fig. 1. Figures 8a and d illustrate the thermohaline vertical sections observed by the buoy during this period, and reveal significant vari-

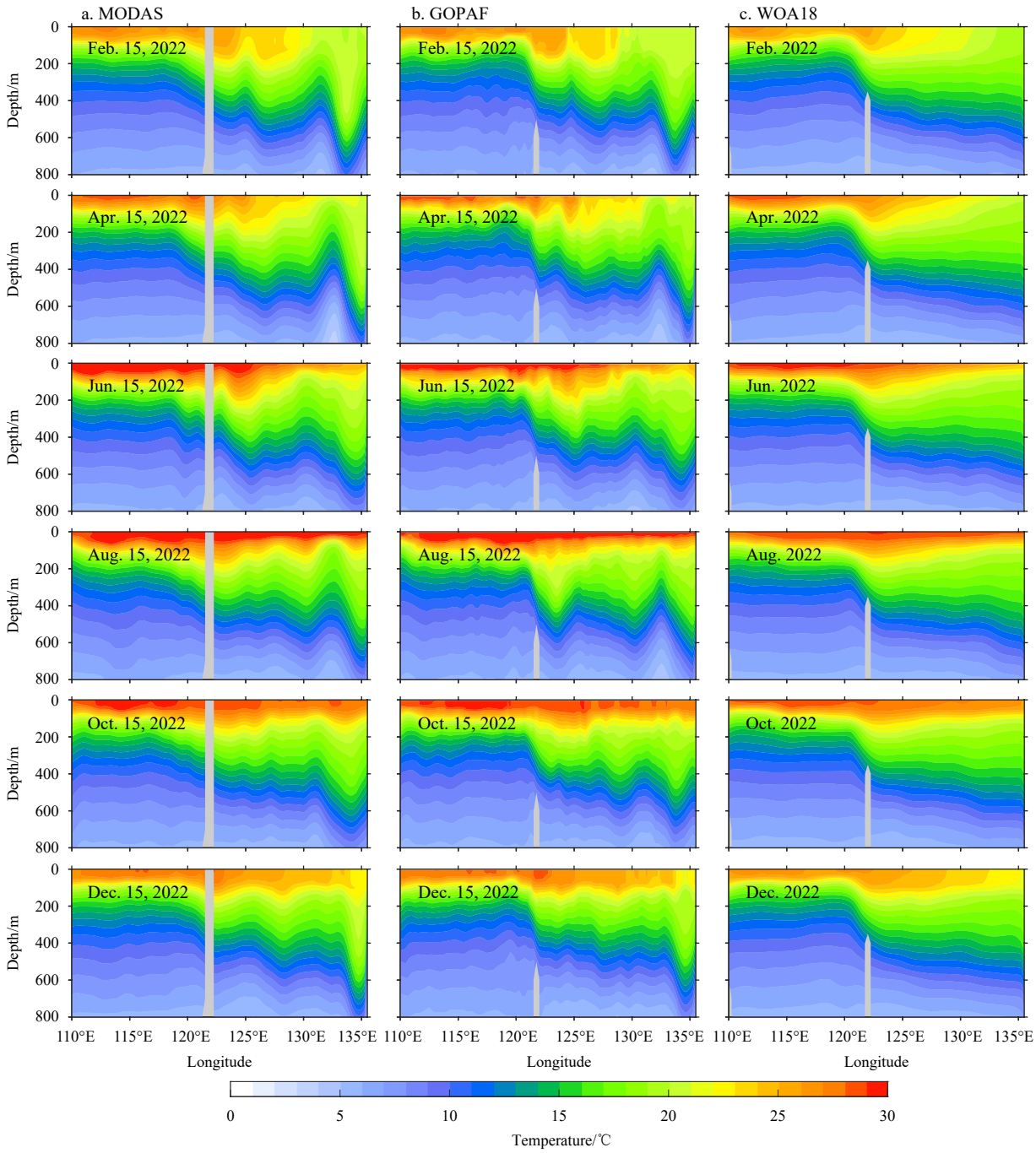


**Fig. 6.** Vertical sections of the MODAS-reconstructed temperature field (a), the GOPAF product's temperature field (b), and the WOA18 monthly climatology temperature field (c) on the 15th day every two months from February to December 2022. The location of these vertical sections is shown in Fig. 5. MODAS, Modular Ocean Data Assimilation System; GOPAF, global ocean physics analysis and forecast; WOA18, World Ocean Atlas 2018.

ations in subsurface thermohaline structure induced by mesoscale processes. The isothermal depths exhibit noticeable fluctuations during the periods of May to June and October to December, corresponding to periods of significant mesoscale processes (Figs 8a and d). In general, the MODAS reconstructed field effectively reproduces these variations in thermohaline structure induced by mesoscale processes, with a maximum $RMSE_T$ of less than 1.5°C, primarily at the second thermocline depth of around 600 m. Regarding salinity, the maximum $RMSE_S$ occurs in the near-surface layer, measuring less than 0.35, and decreases rapidly at depths greater than 150 m (Figs 8b, e and g). The MODAS-reconstructed field has two advantages over the WOA18 monthly climatology field section: (1) the incorporation of SST enhances the temperature reconstruction performance at depths shallower than 100 m; (2) the incorporation of SSH improves the accuracy of temperature and salinity reconstruction at depths greater than the thermocline.

Figure 9 further presents thermohaline anomaly vertical sections. During periods of significant mesoscale processes (e.g., May and June), subsurface warming is more pronounced, with a

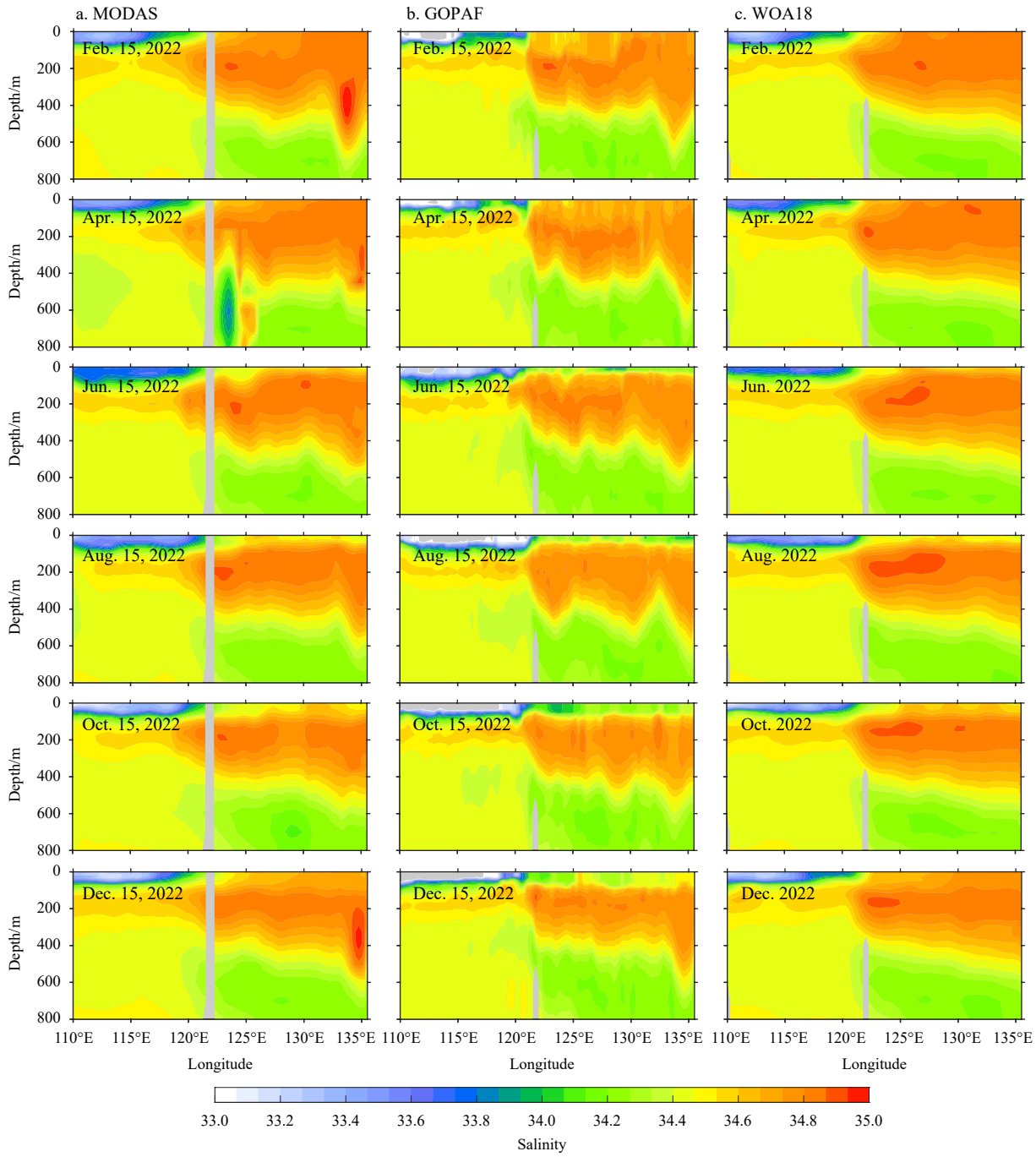


**Fig. 7.** Vertical sections of the MODAS-reconstructed salinity field (a), the GOPAF product's salinity field (b), and the WOA18 monthly climatology salinity field (c) on the 15th day every two months from February to December 2022. The location of the these vertical sections is shown in Fig. 5. MODAS, Modular Ocean Data Assimilation System; GOPAF, global ocean physics analysis and forecast; WOA18, World Ocean Atlas 2018.

maximum anomaly exceeding 4℃ within the range of approximately 400–800 m (Fig. 9b). In comparison to the Argo observations, the MODAS-reconstructed temperature anomaly exhibits a slightly higher magnitude of about 1℃. Still, it demonstrates a similar temperature anomaly structure to the observed section (Fig. 9d). In terms of salinity anomalies, the MODAS reconstructed field shows a maximum subsurface salinity increase of roughly 0.25 from May to June, 2022, which closely aligns with the structure and magnitude of the Argo observation (Figs 9c and e). These results suggest that the MODAS reconstruction method holds promise for describing subsurface thermohaline changes caused by mesoscale processes.

3.2.3 *Estimating the upper ocean response during the TC event*

Previous studies have examined the non-uniform variations in the spatial structure of TC-induced upper ocean temperature anomaly, revealing distinctions between the left and right sides of the TC track. Mei and Pasquero (2013) quantified such asymmetry of SST anomalies response to TC using the methodology outlined in Section 2.5. They delved into the spatial structure and temporal evolution of TC-induced SST anomalies in both pre- and post-TC passage. In the Northern Hemisphere, the surface

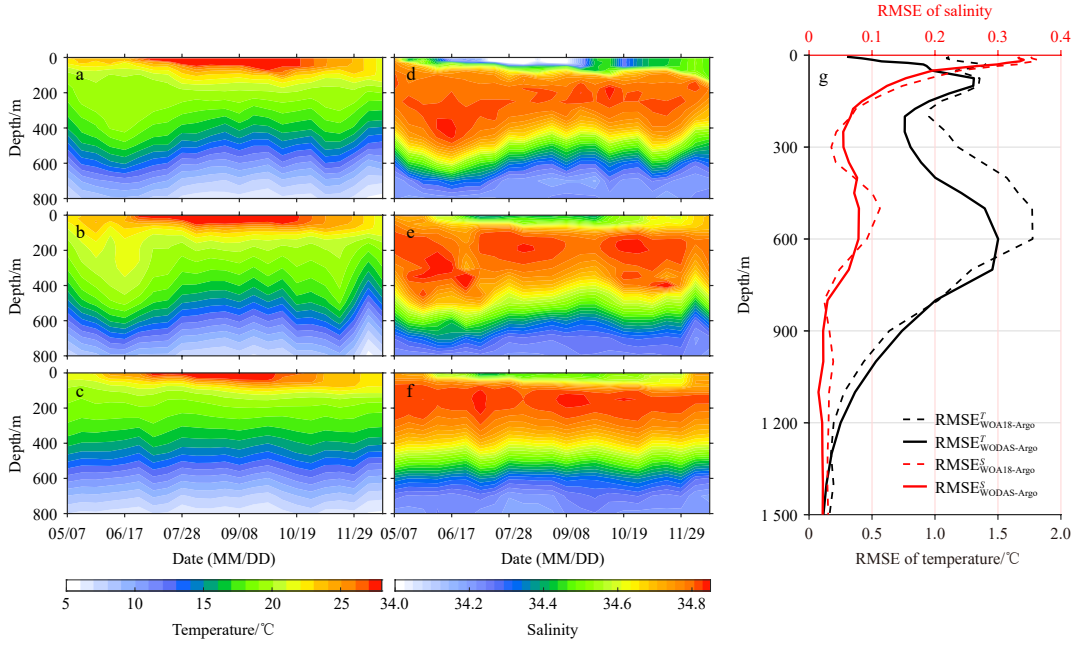


**Fig. 8.** Vertical sections of the Argo-observed (a), the MODAS reconstructed (b), and the WOA18 monthly climatology (c) temperature as a function of depth and time; vertical sections of the Argo-observed (d), the MODAS reconstructed (e), and the WOA18 monthly climatology (f) salinity as a function of depth and time; vertical profiles of RMSE$_T$ (black lines) and RMSE$_S$ (red lines) for MODAS reconstructed (solid lines) and WOA18 monthly climatology fields (dashed lines) (g). MODAS, Modular Ocean Data Assimilation System; WOA18, World Ocean Atlas 2018; RMSE, root mean square error.

(subsurface) cooling (warming) magnitude on the left-hand side of a typical TC track is usually weaker than on the right-hand side. This phenomenon can be attributed to TC-induced vertical mixing in the upper ocean, primarily on the TC track's right-hand side (Price, 1981; Price et al., 1994; Zhou et al., 2019). In our present study, we estimated the upper ocean response during the TC event using the method introduced in Section 2.5, with a first focus on TC Malakas in 2022. The Malakas originated at low latitudes in the NWP and traveled a distance of over 2 000 km from south to north in approximately 7 d, during which it had a noticeable impact on the variation of the subsurface structures in the relevant areas.

Figure 10 depicts the upper ocean subsurface temperature variations based on the MODAS-reconstructed temperature field before and after the passage of Malakas. In this case study, the asymmetry temperature anomaly structure last persistently on both sides of the TC track during different stages. Before Malaka's arrival, subsurface warming is observed on the left-hand side of the TC track within a 400 km range, while cooling is observed on the right side. After the Malakas has passed, significant subsurface cooling occurred on both sides of its path, with the maximum cooling exceeding 1.2℃. Most of this cooling is concentrated in the ocean mixed layer, with the greatest impact observed at depths exceeding 300 m. Six days after the TC passage, the cooling in the ocean surface layer begins to recover gradually. At the same time, there is a general cooling of both the surface and subsurface layers within a radius of about 200 km on both sides of the TC track. However, subsurface warming gradually develops within the 200–400 km range. Furthermore, an asymmetrical pattern emerges, with cooling on the left-hand side and warming on the right-hand side of the TC track with the increase in TC transit time, particularly after the 13th day. During this period, the magnitude of warming on the right side slightly surpasses the cooling on the left side. With time, subsurface warming on the right-hand side takes the lead in returning to normal, and the upper ocean's response to the TC gradually weakened until it eventually disappears.

Given the significant disparities in the intensity of different TC events, we further conducted a composite analysis of the upper ocean response to 26 TC events in the NWP in 2022. The composite results are illustrated in Fig. 11. On average, the TC-induced upper ocean temperature anomaly exhibits varying intensities compared to the single case study, yet notable asymmetry in anomalies persists on both sides of the TC track. Within four days after the TC passage, a subsurface cooling exceeding 0.4℃ is observed within 200 km around the typhoon eye. The cooling extends to depths deeper than 400 m, with its vertical core slightly displaced to the left side of the TC track by 50–100 km. Subsequently, the cooling gradually recovers and swiftly disappears after the 9th day. In regions extending beyond 200 km on the left side of the TC, subsurface warming begins approximately 5 d after the TC passage, with the warming magnitude increasing over time. Simultaneously, the warming on the right side of the TC beyond 200 km is slightly delayed compared to the left side but exhibits a greater magnitude, reaching its peak after 11 d to 14 d and then gradually recovering. This asymmetry in the subsurface temperature structure on both sides of the TC persists throughout the entire stage after the TC passage, showcasing variations in intensity and structure. Such characteristics align with the findings of Cheng et al. (2015). Overall, the case study and the composite analysis results underscore the considerable potential of MODAS reconstructed fields in reproducing the TC-induced upper ocean response.

## 4 Conclusions

In this study, we utilized the autonomous fusion satellite remote sensing SST and SSH observations as inputs to generate operational temperature and salinity products via a statistic-regres-

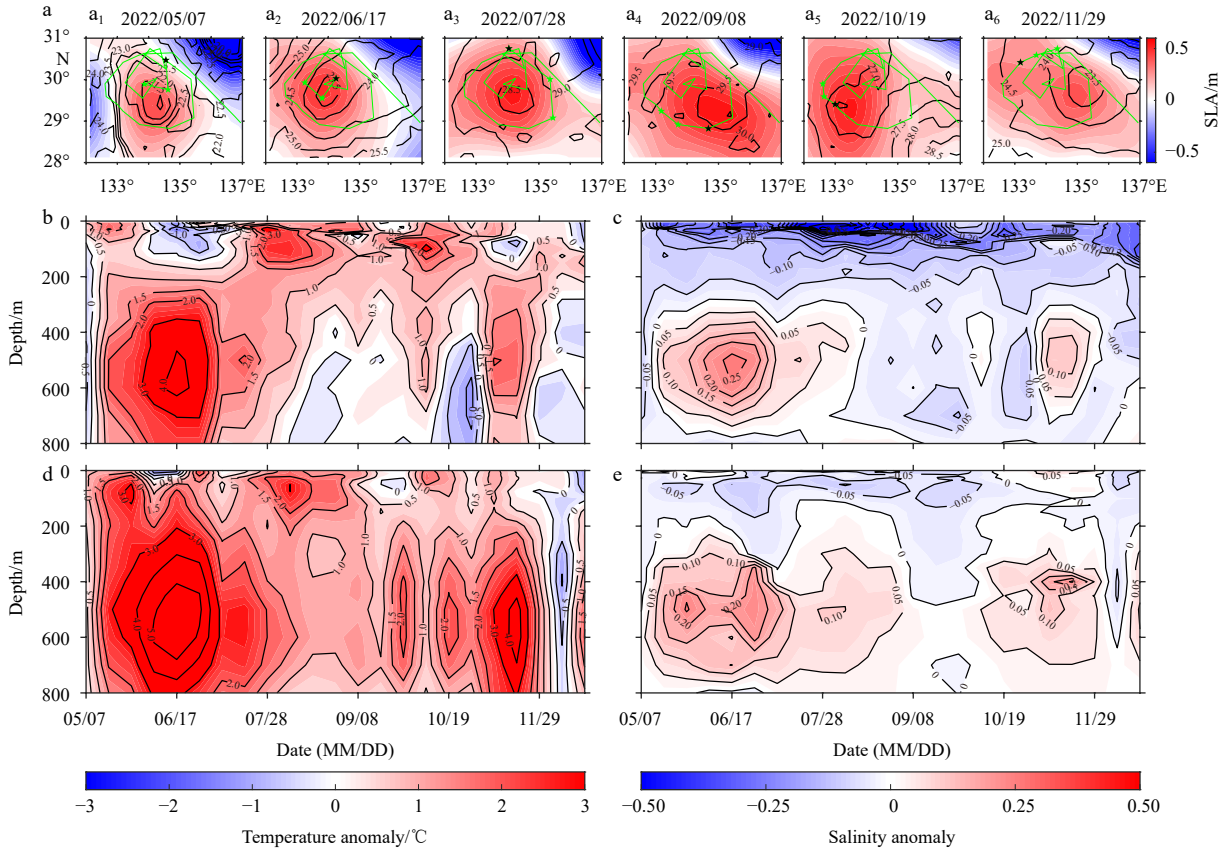


**Fig. 9.** Partial snapshots of sea level anomalies (SLAs, shaded parts) and sea surface temperatures (SSTs, unit in ℃, black contours) during the observation period of Argo buoy No. 5906510 (a), vertical section of temperature anomaly (b) and salinity anomaly (c) of the Argo observation relative to the WOA18 monthly climatology field, and vertical section of temperature anomaly (d) and salinity anomaly (e) of the MODAS-reconstructed field relative to the WOA18 monthly climatology field. For a, the observation date is shown on the top of the subfigures, the green line is the observed trajectory of the buoy between May 7 and December 31, 2022, the green stars indicate the observed positions of the buoy during the specific month (corresponding to the month of the observation date), the black stars are the observed positions of the buoy on the observation date. WOA18, World Ocean Atlas 2018; MODAS, Modular Ocean Data Assimilation System.

sion reconstruction method over the MSR. Several quantitative evaluations are conducted to estimate the reconstructed product, including the reconstruction error statistic analysis, single-point profile comparison, and application in multiscale dynamical processes.

The results of this study demonstrate that the reconstructed temperature and salinity fields surpass the WOA18 monthly climatology field regarding reconstructability, as evidenced by the predominantly positive reconstruction skill scores. Specifically, the $\mathrm{RMSE}_T$ of the reconstructed field remains below 1.5℃ across the MSR, with even smaller values in the NWP, thus highlighting superior reconstruction performance in this region. The high agreement between the reconstructed and observed vertical single-point profiles and vertical sections also reveals that incorporating satellite observations holds promise for reconstructing more accurate upper ocean temperature variations. In addition, the $\mathrm{RMSE}_S$ is lower in the entire MSR and NWP than the NIO, but all the values generally fall below 0.3 at depths greater than the mixed layer. However, the salinity reconstruction exhibits little improvement in the NIO compared to the reconstructed field in the climatology field, which warrants further explorations. Overall, the reconstructed thermohaline fields are expected to provide essential ocean subsurface information for ocean subsurface dynamical environmental estimation within the MSR. They are also expected to serve as the initial field in regional ocean models and be assimilated into numerical reanalysis and prediction systems. This will improve their output, particularly when *in-situ* subsurface observations are lacking.

Next, we applied the reconstructed thermohaline field to reproduce multiscale dynamical processes. Our operational thermohaline product reasonably reproduces stable seasonal variations in subsurface temperature and salinity structures, while the climatology field tends to underestimate these variations. Regarding reproducing thermohaline structure changes induced by mesoscale processes, the reconstructed field excels in characterizing thermocline dynamics and reproducing the subsurface warming induced by mesoscale processes. Nevertheless, there is room for improvement in the accuracy of MODAS-reconstructed near-surface salinity. One potential avenue for enhancing accuracy involves incorporating satellite-observed salinity into the reconstruction model to establish a more refined temperature-salinity relationship. However, the current quality of satellite-derived salinity observations exhibits considerable uncertainty and spatiotemporal variations (Bao et al., 2019; Yan et al., 2021b), posing a challenge in accurately gauging the extent of improvement achievable by incorporating salinity data. Therefore, efforts should be directed towards initially improving the accuracy and stability of salinity observations in future work. Subsequent ex-

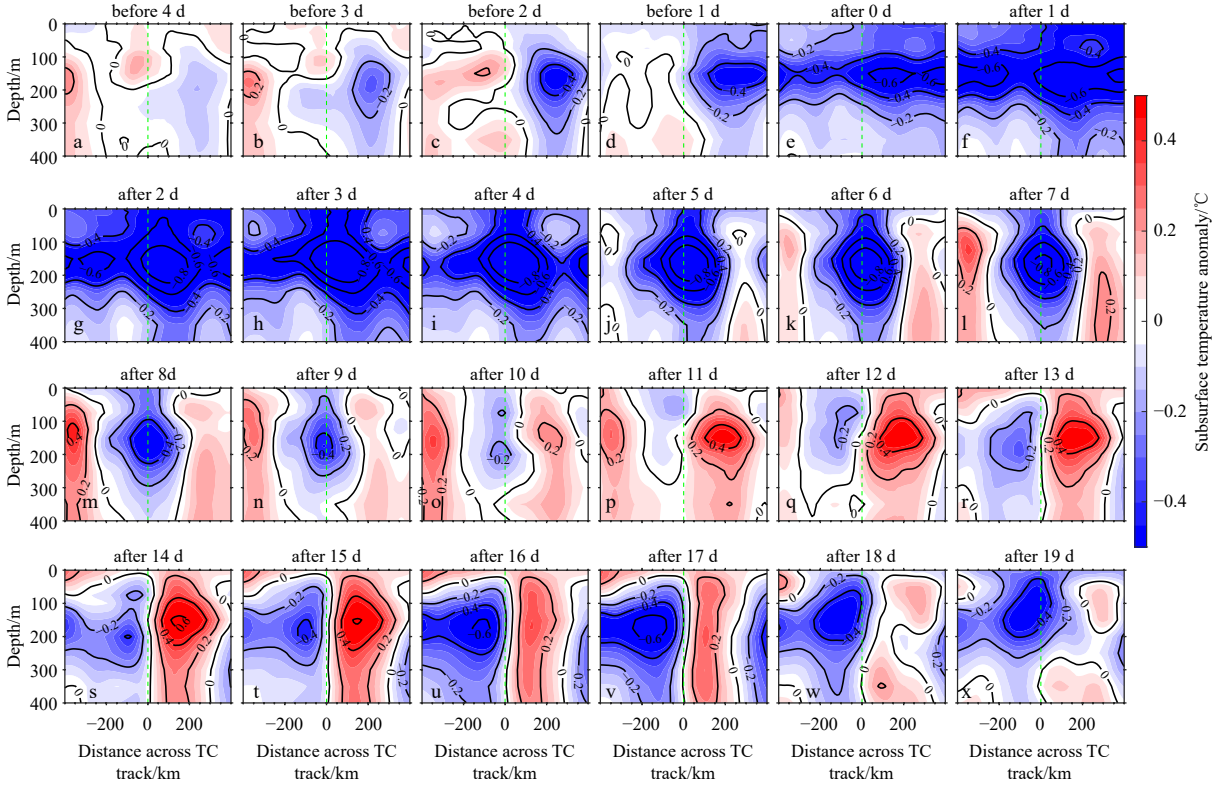


**Fig. 10.** Subsurface temperature anomaly within 400 km across the left-hand (distance less than 0) and right-hand (distance greater than 0) sides of the typhoon track before and after the typhoon's passage. The green dashed line indicates the eye of the tropical cyclone.

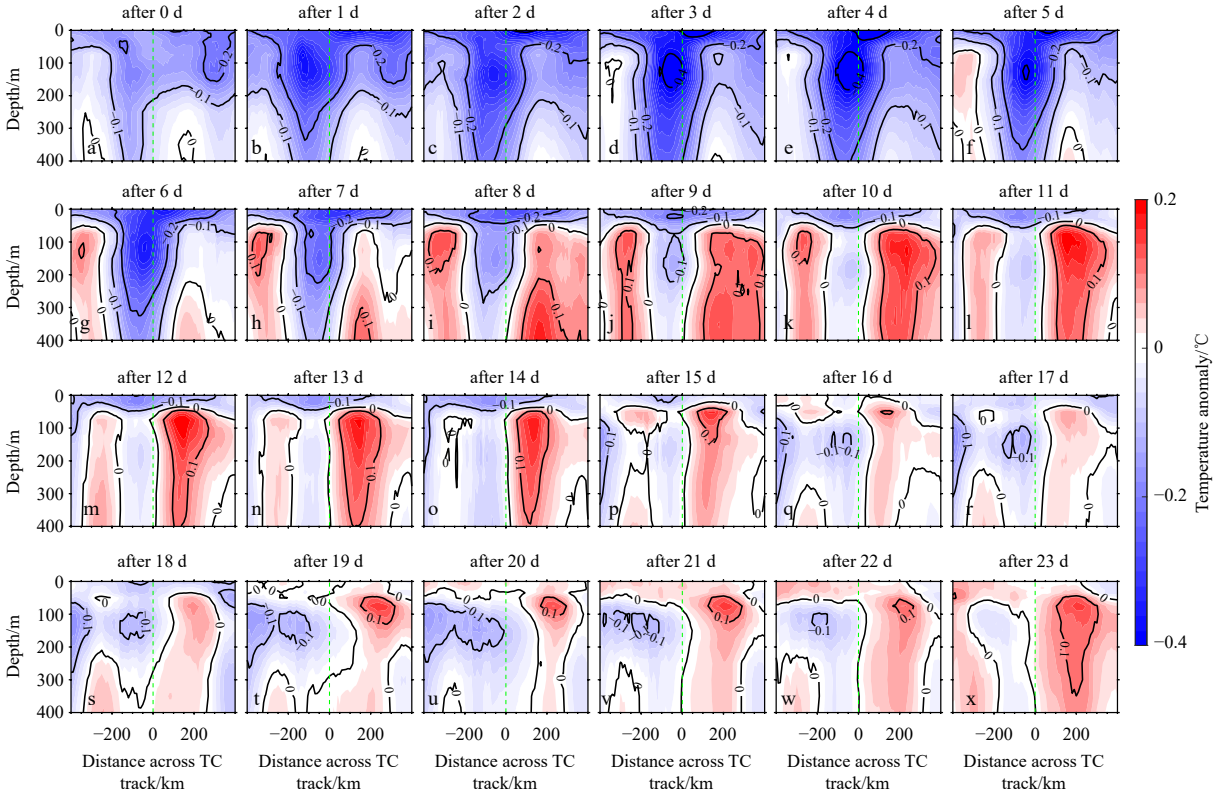


**Fig. 11.** A composite temperature anomaly within 400 km across the left-hand (distance less than 0) and right-hand (distance greater than 0) sides before and after the typhoon's passage for all tropical cyclones (TCs) in the North Indian Ocean in 2022. The green dashed line indicates the eye of the TC.

ploration is warranted to quantify the extent to which salinity observations contribute to the enhanced reconstructability of subsurface salinity.

Our study of TC Malakas and a composite analysis in 2022 allows us to examine the upper ocean's response during extreme weather events. The reconstructed temperature field effectively reproduces subsurface variations before and after the TC passage, revealing asymmetrical variations on both sides of the TC track during different periods. The results of these observations indicate that our reconstructed field can provide a reasonable 3D temperature structure of the ocean during extreme weather events, which is crucial for enhancing the predictive capabilities of marine environmental operational systems during extreme weather events. The results also offer valuable insights regarding the ocean's response to extreme weather events.

***Acknowledgements***

The NSOAS distributes the autonomous satellite remote sensing SSH and SST maps, and can be accessed at https://osdds.nsoas.org.cn. The historical thermohaline profile observations of WOD18 were obtained from https://www.ncei.noaa.gov/products/world-ocean-database. The Argo thermohaline profile observations were accessed at ftp://ftp.ifremer.fr/ifremer/argo/geo/. The Operational Mercator global ocean analysis dataset is from the Copernicus Marine Service (2023). The WOA18 monthly climatology thermohaline field is from the National Centers for Environmental Information (2023). Finally, the typhoon track data and maximum wind speed data can be accessed at https://www.ncei.noaa.gov/products/international-best-track-archive. Xidong Wang acknowledges support from the Laoshan Laboratory.

**References**

Ballabrera-Poy J, Mourre B, Garcia-Ladona E, et al. 2009. Linear and non-linear *T*-*S* models for the eastern North Atlantic from Argo data: Role of surface salinity observations. Deep-Sea Research Part I: Oceanographic Research Papers, 56(10): 1605–1614, doi: 10.1016/j.dsr.2009.05.017

Ballarotta M, Ubelmann C, Veillard P, et al. 2023. Improved global sea surface height and current maps from remote sensing and in situ observations. Earth System Science Data, 15(1): 295–315, doi: 10.5194/essd-15-295-2023

Bao Senliang, Wang Huizan, Zhang Ren, et al. 2019. Comparison of satellite-derived sea surface salinity products from SMOS, aquarius, and SMAP. Journal of Geophysical Research: Oceans, 124(3): 1932–1944, doi: 10.1029/2019JC014937

Buongiorno Nardelli B, Guinehut S, Pascual A, et al. 2012. Towards high resolution mapping of 3-D mesoscale dynamics from observations. Ocean Science, 8(5): 885–901, doi: 10.5194/os-8-885-2012

Burnett W, Harper S, Preller R, et al. 2014. Overview of operational ocean forecasting in the US Navy: past, present, and future. Oceanography, 27(3): 24–31, doi: 10.5670/oceanog.2014.65

Carnes M R, Mitchell J L, De Witt P W. 1990. Synthetic temperature profiles derived from Geosat altimetry: Comparison with air-dropped expendable bathythermograph profiles. Journal of Geophysical Research: Oceans, 95(C10): 17979–17992, doi: 10.1029/JC095iC10p17979

Chen Gengxin, Hou Yijun, Chu Xiaoqing. 2011. Mesoscale eddies in the South China Sea: Mean properties, spatiotemporal variability, and impact on thermohaline structure. Journal of Geophysical Research: Oceans, 116(C6): C06018, doi: 10.1029/2010JC006716

Chen Zhiqiang, Wang Xidong, Liu Lei. 2020. Reconstruction of three-dimensional ocean structure from sea surface data: an application of isQG method in the Southwest Indian Ocean. Journal of Geophysical Research: Oceans, 125(6): e2020jc016351, doi: 10.1029/2020JC016351

Chen Zhiqiang, Wang Xidong, Liu Lei, et al. 2023. Estimating three-dimensional structures of eddy in the South Indian Ocean from the satellite observations based on the isQG method. Earth and Space Science, 10(10): e2023EA002991, doi: 10.1029/2023EA002991

Cheng Lijing, Zhu Jiang, Sriver R L. 2015. Global representation of tropical cyclone-induced short-term ocean thermal changes using Argo data. Ocean Science, 11(5): 719–741, doi: 10.5194/os-11-719-2015

Copernicus Marine Service. 2023. Global ocean physics analysis and forecast. https://data.marine.copernicus.eu/product/GLOBAL_ANALYSISFORECAST_PHY_001_024/description [2023-11-30/2023-12-29], doi: 10.48670/moi-00016

Dash P, Ignatov A, Martin M, et al. 2012. Group for high resolution sea surface temperature (GHRSST) analysis fields inter-comparisons—Part 2: Near real time web-based level 4 SST Quality Monitor (L4-SQUAM). Deep-Sea Research Part II: Topical Studies in Oceanography, 77–80: 31–43, doi: 10.1016/j.dsr2.2012.04.002

Dong Changming, Xu Guangjun, Han Guoqing, et al. 2022. Recent developments in artificial intelligence in oceanography. Ocean-Land-Atmosphere Research, 2022: 9870950, doi: 10.34133/2022/9870950

Dong Chao, Chen Dake, Wang Dongxiao, et al. 2023. Intelligent swift ocean observing system. Ocean-Land-Atmosphere Research, 2: 0022., doi: 10.34133/olar.0022

Fox D N, Teague W J, Barron C N, et al. 2002. The modular ocean data assimilation system (MODAS). Journal of Atmospheric and Oceanic Technology, 19(2): 240–252, doi: 10.1175/1520-0426(2002)019<0240:TMODAS>2.0.CO;2

Guinehut S, Dhomps A L, Larnicol G, et al. 2012. High resolution 3-D temperature and salinity fields derived from *in situ* and satellite observations. Ocean Science, 8(5): 845–857, doi: 10.5194/os-8-845-2012

Guinehut S, Le Traon P Y, Larnicol G, et al. 2004. Combining Argo and remote-sensing data to estimate the ocean three-dimensional temperature fields—a first approach based on simulated observations. Journal of Marine Systems, 46(1–4): 85–98, doi: 10.1016/j.jmarsys.2003.11.022

He Zikang, Wang Xidong, Wu Xinrong, et al. 2021. Projecting three-dimensional ocean thermohaline structure in the North Indian Ocean from the satellite sea surface data based on a variational method. Journal of Geophysical Research: Oceans, 126(1): e2020JC016759, doi: 10.1029/2020JC016759

Huang Longyu, Yang Jingsong, Ma Zetai, et al. 2023. High-frequency observations of oceanic internal waves from geostationary orbit satellites. Ocean-Land-Atmosphere Research, 2: 0024., doi: 10.34133/olar.0024

Hurlburt H E. 1986. Dynamic transfer of simulated altimeter data into subsurface information by a numerical ocean model. Journal of Geophysical Research: Oceans, 91(C2): 2372–2400, doi: 10.1029/JC091iC02p02372

Isern-Fontanet J, Ballabrera-Poy J, Turiel A, et al. 2017. Remote sensing of ocean surface currents: A review of what is being observed and what is being assimilated. Nonlinear Processes in Geophysics, 24(4): 613–643, doi: 10.5194/npg-24-613-2017

Isern-Fontanet J, Lapeyre G, Klein P, et al. 2008. Three-dimensional reconstruction of oceanic mesoscale currents from surface information. Journal of Geophysical Research, 113(C9): C09005, doi: 10.1029/2007JC004692

Knapp K R, Kruk M C, Levinson D H, et al. 2010. The international best track archive for climate stewardship (IBTrACS): Unifying tropical cyclone data. Bulletin of the American Meteorological Society, 91(3): 363–376., doi: 10.1175/2009BAMS2755.1

Liu Lei, Peng Shiqiu, Huang Ruixin. 2017. Reconstruction of ocean's interior from observed sea surface information. Journal of Geophysical Research: Oceans, 122(2): 1042–1056, doi: 10.1002/2016JC011927

Liu Lei, Xue Huijie. 2022. Estimating the Ocean Interior from Satellite Observations in the Kerguelen Area (Southern Ocean): A combined investigation using high-resolution CTD data from

animal-borne instruments. Journal of Physical Oceanography, 52(10): 2463–2478, doi: 10.1175/JPO-D-21-0183.1

Liu Lei, Yu Xiaolong, Xue Huijie, et al. 2023. Reconstructability of open-ocean upper-layer dynamics from surface observations using surface quasigeostrophy (SQG) theory. Journal of Geophysical Research: Oceans, 128(12): e2023JC020124., doi: 10.1029/2023JC020124

Ma Zhanhong, Fei Jianfang, Huang Xiaogang, et al. 2018. Modulating effects of mesoscale oceanic eddies on sea surface temperature response to tropical cyclones over the Western North Pacific. Journal of Geophysical Research: Atmospheres, 123(1): 367–379., doi: 10.1002/2017JD027806

Martin M, Dash P, Ignatov A, et al. 2012. Group for high resolution sea surface temperature (GHRSST) analysis fields inter-comparisons. Part 1: A GHRSST multi-product ensemble (GMPE). Deep-Sea Research Part II: Topical Studies in Oceanography, 77–80: 21–30, doi: 10.1016/j.dsr2.2012.04.013

Mei Wei, Pasquero C. 2013. Spatial and temporal characterization of sea surface temperature response to tropical cyclones. Journal of Climate, 26(11): 3745–3765, doi: 10.1175/JCLI-D-12-00125.1

Morrow R, Fu L L, Ardhuin F, et al. 2019. Global observations of fine-scale ocean surface topography with the surface water and ocean topography (SWOT) mission. Frontiers in Marine Science, 6: 232, doi: 10.3389/fmars.2019.00232

Mulet S, Rio M H, Mignot A, et al. 2012. A new estimate of the global 3D geostrophic ocean circulation based on satellite data and in-situ measurements. Deep-Sea Research Part II: Topical Studies in Oceanography, 77–80: 70–81, doi: 10.1016/j.dsr2.2012.04.012

Nan Feng, He Zhigang, Zhou Hui, et al. 2011. Three long-lived anticyclonic eddies in the northern South China Sea. Journal of Geophysical Research: Oceans, 116(C5): C05002, doi: 10.1029/2010JC006790

National Centers for Environmental Information. 2023. WOA 2018 Data Access: Statistical mean of temperature on 1° grid for all decades. https://www.ncei.noaa.gov/products/world-ocean-atlas [2018-09-30/2023-12-29]

Price J F. 1981. Upper ocean response to a hurricane. Journal of Physical Oceanography, 11(2): 153–175, doi: 10.1175/1520-0485(1981)011<0153:UORTAH>2.0.CO;2

Price J F, Sanford T B, Forristall G Z. 1994. Forced stage response to a moving hurricane. Journal of Physical Oceanography, 24(2): 233–260, doi: 10.1175/1520-0485(1994)024<0233:FSRTAM>2.0.CO;2

Qiao Fangli, Wang Guansuo, Khokiattiwong S, et al. 2019. China published ocean forecasting system for the 21st-Century Maritime Silk Road on December 10, 2018. Acta Oceanologica Sinica, 38(1): 1–3, doi: 10.1007/s13131-019-1365-y

Qiu Bo, Chen Shuiming, Klein P, et al. 2014. Seasonal mesoscale and submesoscale eddy variability along the North Pacific subtropical countercurrent. Journal of Physical Oceanography, 44(12): 3079–3098, doi: 10.1175/JPO-D-14-0071.1

Riser S C, Freeland H J, Roemmich D, et al. 2016. Fifteen years of ocean observations with the global Argo array. Nature Climate Change, 6(2): 145–153, doi: 10.1038/nclimate2872

Su Hua, Lu Wenfang, Wang An, Zhang Tianyi. 2023. Al-based subsurface thermohaline structure retrieval from remote sensing observations. In: Li Xiaofeng, Wang Fan, eds, Artificial Intelligence Oceanography. Singapore: Springer Nature Singapore, 105–123, doi: 10.1007/978-981-19-6375-9_5

Tang Bo, Zhao Dandan, Cui Chaoran, et al. 2022. Reconstruction of ocean temperature and salinity profiles in the northern South China Sea using satellite observations. Frontiers in Marine Science, 9: 945835, doi: 10.3389/fmars.2022.945835

Wang Xidong, Chu P C, Han Guijun, et al. 2012a. A fully conserved minimal adjustment scheme with ($T$, $S$) coherency for stabilization of hydrographic profiles. Journal of Atmospheric and Oceanic Technology, 29(12): 1854–1865, doi: 10.1175/JTECH-D-12-00025.1

Wang Xidong, Li Wei, Qi Yiquan, et al. 2012b. Heat, salt and volume transports by eddies in the vicinity of the Luzon Strait. Deep-Sea Research Part I: Oceanographic Research Papers, 61: 21–33, doi: 10.1016/j.dsr.2011.11.006

Xie Huarong, Xu Qing, Cheng Yongcun, et al. 2022. Reconstruction of subsurface temperature field in the south china sea from satellite observations based on an attention U-Net model. IEEE Transactions on Geoscience and Remote Sensing, 60: 4209319, doi: 10.1109/TGRS.2022.3200545

Yan Hengqian, Zhang Ren, Wang Huizan, et al. 2021a. A surface quasi-geostrophic—based dynamical-statistical framework to retrieve interior temperature/salinity from ocean surface. Journal of Geophysical Research: Oceans, 126(10): e2020JC017139, doi: 10.1029/2020JC017139

Yan Hengqian, Wang Huizan, Zhang Ren, et al. 2021b. The inconsistent pairs between *in situ* observations of near surface salinity and multiple remotely sensed salinity data. Earth and Space Science, 8(5): e2020EA001355, doi: 10.1029/2020EA001355

Yang Yikai, Wang Dongxiao, Wang Qiang, et al. 2019. Eddy-induced transport of saline kuroshio water into the northern South China Sea. Journal of Geophysical Research: Oceans, 124(9): 6673–6687, doi: 10.1029/2018JC014847

Zhou Lei, Chen Dake, Lei Xiaotu, et al. 2019. Progress and perspective on interactions between ocean and typhoon. Chinese Science Bulletin, 64(1): 60–72, doi: 10.1360/N972018-00668